AUT Journal of Mechanical Engineering

AUT J. Mech. Eng., 6(1) (2022) 59-76
DOI: 10.22060/ajme.2021.19915.5972

Nonlinear Flutter Analysis of Porous Functionally Graded Plate in Yawed Hypersonic Flow

M. Javadi*, V. Khalafi

Department of Aerospace Engineering, Shahid Sattari Aeronautical University of Science and Technology, Tehran, Iran

ABSTRACT: In this paper, an aerothermoelastic analysis of functionally graded plate containing porosities in yawed hypersonic flows is investigated. Due to some incorrect manufacturing processes, two different types of porosity, namely, even and uneven distributions are taken into account. The third-order piston theory is utilized to estimate the unsteady aerodynamic pressure induced by the hypersonic airflow. The material properties of a plate are assumed to vary across the thickness direction according to a simple power law. Based on classical plate theory, the motion equations are developed with geometric nonlinearity taking into consideration of von Karman strains. The formulations are established based on Hamilton's principle while the generalized differential quadrature method is employed to solve the nonlinear aerothermoelastic equations. Due to lower computational efforts, the method of generalized differential quadrature is used to obtain accurate results. Moreover, the assumed mode method along with the Runge-Kutta integration algorithm is used as a solution method. The reliability and precision of the obtained results are validated by published literature. Then, the influence of porosity distribution, porosity coefficient, and yawed flow angle are discussed in detail. In general, this paper shows that even porosity distribution would have a more destabilizing effect compared with the uneven porous model. And also, for both porosity distributions, the chaotic behavior appears in higher top surface temperature but even porosity distribution has a profound effect on chaotic motion.

Review History:

Received: Apr. 23, 2021
Revised: Sep, 14, 2021
Accepted: Sep, 15, 2021
Available Online: Sep, 19, 2021

Keywords:

Functionally graded porous
Yawed hypersonic airflow
Bifurcation
Differential quadrature method
Aerothermoelastic

1- Introduction

The Functionally Graded Material (FGM) is a newfangled composite material that is produced of two or more constituent phases with a continuous variation of material properties to reduce the stress intensity observed in the conventional laminated composites [1]. The FGM structures are extensively employed in aerospace engineering due to their great performances in simultaneous mechanical, aerodynamic, and thermal loadings. The panel flutter phenomenon is a kind of dynamic instability problem inflight space vehicles with high speed, which critically influences the skin structures and generally induces fatigue failure [2]. Therefore, it is necessary and meaningful for investigators to analyze the aerothermoelastic of FGM plates. Piston theory is an applied tool for estimating aerodynamic force dealing with the aeroelasticity issue of aerospace structures. In the supersonic regime, the first-order piston is suitable and predicts only the threshold of flutter and provides no sign over the post-flutter instability zone. But, in the hypersonic regime, the nonlinear coupling effects are a key factor in the aeroelastic response [3, 4].

Studies on flutter behaviors of plates and shells have been performed in the past years [5]. Across the consecutive progress of FGMs, numerous examinations have been conducted on flutter problems until now. The thermal effects are essential since the temperature environment causes dramatic influences on the static and dynamic behaviors of flight structures in supersonic/hypersonic regimes [6]. Aeroelastic study of FG flat panels including thermal effects was studied by Prakash and Ganapathi [7]. Sohn and Kim [8] investigated divergence and flutter stability of FG panels including thermal effects. It is claimed the critical dynamic pressures for the flutter of FG panels are also higher than that of isotropic metal panels. Li and Song [9] analyzed the aerothermoelastic properties of laminated panels. They found the outer layer ply angle of the laminated panel is more important than that of the inner layer for the flutter instability. The aerothermoelastic behavior of composite laminated trapezoidal panels considering the compressibility of supersonic airflow and shock wave were studied by Jiang and Li [10]. They realized, by increasing the ply-angle, the critical buckling temperature rises first and then reduces quickly. Khalafi and Fazilati [11] investigated aeroelastic analysis of variable stiffness composite laminated skew panels exposed to yawed airflow. It is claimed the fiber orientations role at two ends of the Variable Stiffness Composite Laminated (VSCL) skew plate on its instability behavior is remarkable.

*Corresponding author's email: javadi@ssau.ac.ir

Aeroelastic analysis of elastically restrained stiffened FG plates including the thermal environment was studied by Su et al. [2]. They showed the enhancement of elastic restraints increase frequency parameters and critical aerodynamic pressure. The effect of the boundary relaxation on the flutter instability and divergence of composite laminated panels was examined by Chai et al. [12]. The influence of in-plane stresses on the aeroelastic characteristic of constant stiffness and variable stiffness composite panels, subjected to supersonic airflow, was studied by Rasool and Singha [13]. It is claimed the constant-stiffness cross-ply laminates suggest more endurance to flutter instability for the case of square composite plates. Supersonic flutter analysis of a laminated composite plate by considering material uncertainty was examined by Swain and et al. [14]. They found the perturbation technique is highly efficient than the conventional Monte Carlo simulation method. It should be mentioned that these aforesaid publications are approximately limited to the number of approximate methods such as the Rayleigh-Ritz method, Galerkin method, finite element method, and the differential quadrature method [15]. The linear and the nonlinear deformation behavior of FG spherical shell panels are examined by Kar and Panda [16]. They found with the increase in curvature ratio, the deflection parameters increase under mechanical load, however, a reverse trend is found in the case of thermo-mechanical load.

Up to now, few scholars have been carried out on the nonlinear complication of the post-flutter zone, which is crucial for aerospace structure [17]. The nonlinear flutter behavior of a two-dimensional simply supported symmetric composite laminated plate was investigated by [18]. They used Von Karman's large deflection plate theory for structural dynamics, first-order piston theory for aerodynamic forces, and applied the Galerkin method to decrease the governing equations to a set of nonlinear ordinary differential equations in time. Ibrahim et al. [19] studied aerothermoelastic analysis for temperature-dependent FGM panels. They also utilized the first-order piston theory to model aerodynamic pressure. Sohn and Kim investigated the nonlinear thermal flutter of functionally graded panels under a supersonic flow. They used the Newton–Raphson method to obtain approximate solutions. The problem of nonlinear aeroelasticity of a general laminated composite plate in supersonic airflow was examined by Kouchakzadeh et al. [20]. They obtained the aerodynamic damping has a more significant influence on Limit Cycle Oscillation (LCO) amplitude for small fiber angles and high aerodynamic pressures. Navazi and Haddadpour [21] studied nonlinear flutter investigation of homogeneous and FGM plates in supersonic airflow utilizing coupled models. Aerothermoelastic analysis of nonlinear composite laminated panel with aerodynamic heating in hypersonic flow was investigated by Song and Li [22]. They showed with the increase of the dimensionless aerodynamic pressure, the LCO amplitude of the panel increases, which means that the aeroelastic stability is declined, and it will be intensified if the thermal influence is considered. Shahverdi and Khalafi [23] showed that the post-flutter behavior of a functionally graded curved panel may be led to a chaotic motion in presence of thermal loads. Chai et al. [24] studied the nonlinear dynamic characteristics of lattice sandwich composite panels resting on Winkler–Pasternak elastic foundations under simultaneous aerodynamic and thermal loads in supersonic airflow. They found the Winkler foundation cannot enhance the flutter bounds of the lattice sandwich composite panel effectively. Xia et al. [25] found the asymmetry of FG material has little effect on the simple harmonic LCO flutterbut has significant effects on the non-simple harmonic LCO flutter. Ye and Ye [26] showed the temperature-dependent variation of the thermal expansion coefficient has a crucial effect on reducing the critical buckling temperature elevation.

Furthermore, porosities are a quite common phenomenon in functionally graded materials due to incorrect manufacturing processes and technical problems [27-30]. Duc et al. [31] studied the nonlinear dynamic response of functionally graded plates with porosities on the elastic foundation. The aeroelastic analysis of FGM plate with porosities in the thermal environment and resting on elastic foundations was studied by Zhou et al. [32]. The observed influence of porosity may lead to a decrease of stability margin when the plate is subjected to large thermal loads. The aeroelastic flutter analysis of thick plates with porosities which is surrounded by piezoelectric layers in supersonic flow was studied by Bahaadini et al. [33]. They found the natural frequencies, as well as flutter aerodynamic pressure of thick FG plates with porosities, reduce as the coefficient porosity expansions.

Rahmanian et al. [34] investigated the aeroelastic stability of tapered/skew variable stiffness composite cantilevered plates. They found taperness/skewness, as well as variable stiffness lamination parameters, have significant effects on the aeroelastic stability margins.

From the review of the literature, we can conclude that the study of coupled nonlinear geometric structure and nonlinear piston theory (third-order) are limited, and nonlinear flutter analysis of porous functionally graded plate in yawed hypersonic flow has not been addressed in the existing open literature.

The objective of this paper is to investigate the critical flutter point and nonlinear flutter of a porous functionally graded plate that is subjected to yawed hypersonic flow. Material properties of the functionally graded plate are dependent on temperature and the distribution of their constituents are graded along thickness direction by a simple power law. Two types of FG porous distributions, namely even porosity and uneven porosity distribution was considered in this paper. The third-order piston theory is used to calculate the aerodynamic force. Hamilton's principle is employed to formulate the equations of motion. Based on the generalized differential quadrature method, the nonlinear aerothermoelastic equation is transferred to ordinary differential equations. Moreover, the assumed mode method along with the Runge-Kutta integration algorithm is used as a solution method.

The manuscript is organized as follows. In Section 2,

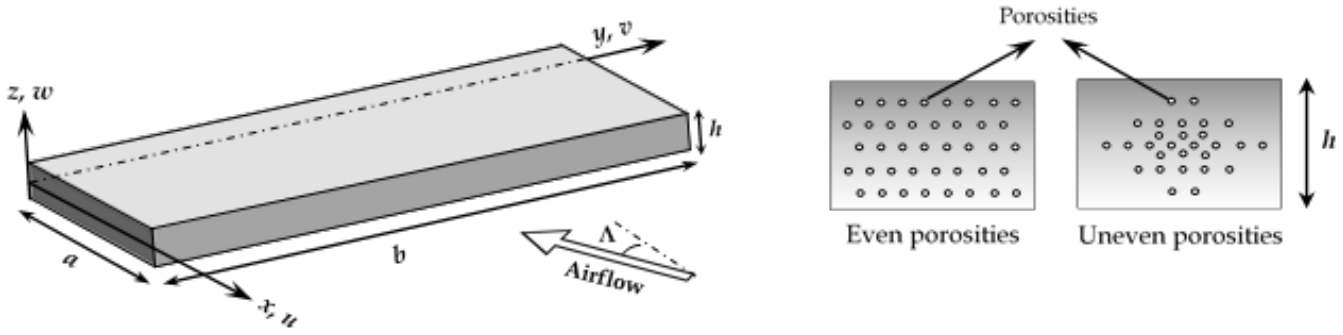

Fig. 1. Geometry and coordinate system of an FGM plate with porosities in hypersonic airflow.

material properties, porous distributions, and the third-order piston theory is presented. Based on von Karman's nonlinear hypothesis, the aeroelastic equations of a Functionally Graded Porous (FGP) plate are proposed in Section 3. The method of Generalized Differential Quadrature (GDQM) is introduced in Section 4 and this method is used to discretize the aeroelastic equation. Finally, some important conclusions are drawn in Section 5.

2- Theory and Formulation

2- 1- Structural model

The schematic view of a porous FGM plate with a length a, width b, and thickness h which is subjected to a hypersonic airflow is demonstrated in Fig. 1. The Cartesian coordinate (x; y; z) is located on the mid-surface of the plate. Variables u, v, and w represent the displacements of an arbitrary point of the rectangular plate in x, y, and z directions, respectively.

The plate is made of functionally graded material in the thickness direction. The temperature-dependent properties of constituent materials can be written as follows [7]

$$P = P_0 \ P_{-1}T^{-1} + 1 + P_1T + P_2T^2 + P_3T^3 \ , \tag{1}$$

where P_0, P_{-1}, P_1, P_2, and P_3 are the temperature coefficients of the constituent materials, and T is the Kelvin temperature.

As presented in Fig. 1, two types of porosity distributions along the thickness direction, namely even and uneven, are considered in this study. The effective material property of the FGM plate takes the modified form as follows [35]:

$$P(z,T) = P_m(T)\left(V_m(z) - \frac{\alpha}{2}\right) + P_c(T)\left(V_c(z) - \frac{\alpha}{2}\right) \tag{2}$$

where α is the porosity volume fraction and P_m and P_c are material properties of metal and ceramic, respectively. V_m and V_c are the volume fractions of metal and ceramic and are related by:

$$V_c + V_m = 1 \tag{3}$$

The volume fractions of the ceramic and the metal can be written as follows

$$V_c(z) = \left(\frac{z}{h} + \frac{1}{2}\right)^n, \qquad V_c + V_m = 1 \tag{4}$$

The continuous variation of the elastic modulus E, the mass density ρ, Poisson's ratio v, and thermal expansion coefficient α_T the thermal conductivity K due to the graded porosity can be described as [29]

For even porosity model:

$$\begin{aligned}
E(z,T) &= E_c(T) - E_m(T)\, V_c + \\
&\quad E_m(T) - \frac{\alpha}{2}\, E_c(T) + E_m(T) \\
\rho(z,T) &= \rho_c(T) - \rho_m(T)\, V_c + \\
&\quad \rho_m(T) - \frac{\alpha}{2}\, \rho_c(T) + \rho_m(T) \\
v(z,T) &= v_c(T) - v_m(T)\, V_c + \\
&\quad v_m(T) - \frac{\alpha}{2}\, v_c(T) + v_m(T) \\
K(z) &= K_c - K_m\, V_c + \\
&\quad K_m - \frac{\alpha}{2}\, K_c + K_m \\
\alpha_T(z,T) &= \alpha_{T,c}(T) - \alpha_{T,m}(T)\, V_c + \\
&\quad \alpha_{T,m}(T) - \frac{\alpha}{2}\, \alpha_{T,c}(T) + \alpha_{T,m}(T)
\end{aligned} \tag{5}$$

For uneven porosity model:

$$
\begin{aligned}
E(z,T) &= E_c(T) - E_m(T)\,V_c + E_m(T) - \\
&\quad \frac{\alpha}{2}\,E_c(T) + E_m(T)\;\;1 - 2|z|/h \\
\rho(z,T) &= \rho_c(T) - \rho_m(T)\,V_c + \rho_m(T) - \\
&\quad \frac{\alpha}{2}\,\rho_c(T) + \rho_m(T)\;\;1 - 2|z|/h \\
\nu(z,T) &= \nu_c(T) - \nu_m(T)\,V_c + \nu_m(T) - \\
&\quad \frac{\alpha}{2}\,\nu_c(T) + \nu_m(T)\;\;1 - 2|z|/h \\
K(z) &= K_c - K_m\,V_c + K_m - \\
&\quad \frac{\alpha}{2}\,K_c + K_m\;\;1 - 2|z|/h \\
\alpha_T(z,T) &= \alpha_{T,c}(T) - \alpha_{T,m}(T)\,V_c + \\
&\alpha_{T,m}(T) - \frac{\alpha}{2}(\alpha_{T,c}(T) + \alpha_{T,m}(T))(1 - 2|z|/h)
\end{aligned}
\tag{6}
$$

For dynamic modeling and deriving the kinetic and potential energy terms for the FGP plate, the following assumptions are made in thin or classical plate theory [36]:

The thickness of the plate (h) is small compared to its lateral dimensions.

The middle plane of the plate does not undergo in-plane deformation.

The displacement of the mid-surface of the plate is small compared to the thickness of the plate.

The influence of transverse shear deformation is neglected.

The transverse normal strain under transverse loading can be neglected.

Based on assumptions of CPT, the following displacement field is presumed,

$$
\begin{aligned}
u(x,y,z,t) &= u_0(x,y,z,t) - z\frac{\partial w_0(x,y,z,t)}{\partial x} \\
v(x,y,z,t) &= v_0(x,y,z,t) - z\frac{\partial w_0(x,y,z,t)}{\partial y} \\
w(x,y,z,t) &= w_0(x,y,t)
\end{aligned}
\tag{7}
$$

where u_0, $v_{0,}$ and w_0 are the displacements on the middle surface of the FGM plate in the x, y, and z directions respectively. To model the geometric nonlinearity due to large deflection, von Karman strain-displacement relations can be expressed as

$$
\begin{Bmatrix} \varepsilon_{xx} \\ \varepsilon_{yy} \\ \varepsilon_{xy} \end{Bmatrix} = \begin{Bmatrix} \varepsilon^0_{xx} \\ \varepsilon^0_{yy} \\ \varepsilon^0_{xy} \end{Bmatrix} + z \begin{Bmatrix} \kappa^0_{xx} \\ \kappa^0_{yy} \\ \kappa^0_{xy} \end{Bmatrix}
\tag{8}
$$

where $\hat{a}^0_{xx}$ and $\hat{a}^0_{yy}$ are normal strains, $\hat{a}^0_{xy}$ is the shear strain at the middle surface of the plate and also $\hat{e}^0_{xx}$, $\hat{e}^0_{yy}$, and $\hat{e}^0_{xy}$ are the bending strains of the middle surface, which can be written as

$$
\begin{Bmatrix} \varepsilon^0_{xx} \\ \varepsilon^0_{yy} \\ \varepsilon^0_{xy} \end{Bmatrix} = \begin{Bmatrix} \dfrac{\partial u_0}{\partial x} \\ \dfrac{\partial v_0}{\partial y} \\ \dfrac{\partial u_0}{\partial y} + \dfrac{\partial v_0}{\partial x} \end{Bmatrix}, \quad \begin{Bmatrix} \kappa^0_{xx} \\ \kappa^0_{yy} \\ \kappa^0_{xy} \end{Bmatrix} = \begin{Bmatrix} -\dfrac{\partial^2 w_0}{\partial x^2} \\ -\dfrac{\partial^2 w_0}{\partial y^2} \\ -2\dfrac{\partial^2 w_0}{\partial x \partial y} \end{Bmatrix}
\tag{9}
$$

The FG plate under the thermal loads will produce thermal strain and thermal stress when the temperature increase $\Delta(z)$, it can be written as,

$$
\begin{Bmatrix} \varepsilon^T_{xx}(z,T) \\ \varepsilon^T_{yy}(z,T) \\ \varepsilon^T_{xy}(z,T) \end{Bmatrix} = -\begin{Bmatrix} \alpha_T \\ \alpha_T \\ 2\alpha_T \end{Bmatrix} \Delta T(z),
\tag{10}
$$

$\Delta(z) = T(z) - T_0$ being the temperature rise from the stress-free temperature (T_0). Based on the plane stress condition, the thermoelastic constitutive for the FGP plate can be written as follows [37]:

$$
\begin{Bmatrix} \sigma_{xx} \\ \sigma_{yy} \\ \sigma_{xy} \end{Bmatrix} = \begin{bmatrix} Q_{11} & Q_{21} & 0 \\ Q_{12} & Q_{22} & 0 \\ 0 & 0 & Q_{66} \end{bmatrix} \left\{ \begin{Bmatrix} \varepsilon_{xx} \\ \varepsilon_{yy} \\ \varepsilon_{xy} \end{Bmatrix} - \begin{Bmatrix} 1 \\ 1 \\ 0 \end{Bmatrix} \alpha_T(z,T)\Delta T \right\}
\tag{11}
$$

where Q_{ij} are the reduced stiffnesses and are defined as

$$
\begin{aligned}
Q_{11} &= Q_{22} = \frac{E(z,T)}{1 - \nu^2(z,T)}, \\
Q_{12} &= \frac{E(z,T)\nu^2(z,T)}{1 - \nu^2(z,T)}, \\
Q_{66} &= \frac{E(z,T)}{2(1 + \nu(z,T))}
\end{aligned}
\tag{12}
$$

The force and moment resultants are defined as

$$
\begin{Bmatrix} \mathbf{N} \\ \mathbf{M} \end{Bmatrix} = \begin{bmatrix} \mathbf{A} & \mathbf{B} \\ \mathbf{B} & \mathbf{D} \end{bmatrix} \begin{Bmatrix} \varepsilon^0 \\ \kappa^0 \end{Bmatrix} - \begin{Bmatrix} \mathbf{N}^T \\ \mathbf{M}^T \end{Bmatrix}
\tag{13}
$$

where the thermal stress resultants vectors, $\mathbf{N}^T$ and $\mathbf{M}^T$ are introduced as:

$$
\begin{aligned}
\mathbf{N}^T &= \begin{Bmatrix} N^T_{xx} \\ N^T_{yy} \end{Bmatrix} = \\
&\int_{-h/2}^{h/2} \begin{bmatrix} Q_{11} & Q_{12} \\ Q_{21} & Q_{22} \end{bmatrix} \begin{Bmatrix} \alpha_T(z,T) \\ \alpha_T(z,T) \end{Bmatrix} \Delta T \; \mathrm{d}z \\
\mathbf{M}^T &= \begin{Bmatrix} M^T_{xx} \\ M^T_{yy} \end{Bmatrix} = \\
&\int_{-h/2}^{h/2} \begin{bmatrix} Q_{11} & Q_{12} \\ Q_{21} & Q_{22} \end{bmatrix} \begin{Bmatrix} \alpha_T(z,T) \\ \alpha_T(z,T) \end{Bmatrix} \Delta T \; z \; \mathrm{d}z
\end{aligned}
\tag{14}
$$

And also $\mathbf{A}_{ij}$, $\mathbf{D}_{ij}$, and $\mathbf{B}_{ij}$ are the extensional, bending, and bending-extensional coupling stiffnesses coefficients given by

$$\begin{aligned} A_{ij} &= \int_{-h/2}^{h/2} Q_{ij} dz, \\ B_{ij} &= \int_{-h/2}^{h/2} Q_{ij} z dz, \\ D_{ij} &= \int_{-h/2}^{h/2} Q_{ij} z^2 dz \end{aligned} \tag{15}$$

2- 2- Aerodynamic modeling

In the present study, the fluid-structure effect due to external aerodynamic pressure loading in a hypersonic regime can be taken into account using third-order piston theory [38]. This pressure is expressed as:

$$\Delta P = 2q\left[\begin{array}{l} \frac{1}{M}\left(\frac{1}{U}\frac{\partial w}{\partial t}+\frac{\partial w}{\partial x}\cos\Lambda+\frac{\partial w}{\partial y}\sin\Lambda\right)+ \\ \frac{\gamma+1}{4}\left(\frac{1}{U}\frac{\partial w}{\partial t}+\frac{\partial w}{\partial x}\cos\Lambda+\frac{\partial w}{\partial y}\sin\Lambda\right)^2+ \\ \frac{\gamma+1}{12}M\left(\frac{1}{U}\frac{\partial w}{\partial t}+\frac{\partial w}{\partial x}\cos\Lambda+\frac{\partial w}{\partial y}\sin\Lambda\right)^3 \end{array}\right] \tag{16}$$

where γ is the adiabatic exponent, U is the free-stream free stream velocity, M is Mach number, Λ is airflow yaw angle (according to Fig. 1) and q is dynamic pressure.

2- 3- Temperature distribution

It is assumed that the temperature varies only across the thickness direction and is also determined by solving the following steady-state one-dimensional heat conduction equation:

$$-\frac{\mathrm{d}}{\mathrm{d}z}\left(K(z)\frac{\mathrm{d}T}{\mathrm{d}z}\right)=0 \tag{17}$$

with the boundary condition

$$T=\begin{cases} T_m, & z=-h/2 \\ T_c, & z=h/2 \end{cases} \tag{18}$$

The solution of the heat conduction equation can be expressed as [32]

$$T = T_m + T_c - T_m \frac{\int_{-h/2}^{z}\frac{1}{K(z)}\mathrm{d}z}{\int_{-h/2}^{h/2}\frac{1}{K(z)}\mathrm{d}z} \tag{19}$$

3- Governing Equations

Based on von Karman's nonlinear hypothesis, the aeroelastic equations of an FGP plate can be formulated utilizing the extended Hamilton's principle [37, 39]. The aeroelastic equations by considering body moments and inertial forces in the x and y directions, and neglecting surface shearing forces, yield:

$$\begin{aligned} &\frac{\partial N_{xx}}{\partial x}+\frac{\partial N_{xy}}{\partial y}=0 \\ &\frac{\partial N_{yy}}{\partial y}+\frac{\partial N_{xy}}{\partial x}=0 \\ &\frac{\partial M_{xx}}{\partial x^2}+2\frac{\partial M_{xy}}{\partial x\,\partial y}+\frac{\partial M_{yy}}{\partial y^2}+N_{xx}\frac{\partial^2 w}{\partial x^2}+ \\ &2N_{xy}\frac{\partial^2 w}{\partial x\,\partial y}+N_y\frac{\partial^2 w}{\partial y^2}+\Delta P=I_0\frac{\partial^2 w}{\partial t^2} \end{aligned} \tag{20}$$

where

$$I_0=\int_{-h/2}^{h/2}\rho(z,T)\mathrm{d}z \tag{21}$$

The governing equations of porous FGM plate under hypersonic airflow loads in terms of the displacement can be obtained by inserting for the force and moment resultants as follows:

$$\begin{aligned} &\left(\frac{\partial^4 w}{\partial x^4}+2\frac{\partial^4 w}{\partial x^2\partial y^2}+\frac{\partial^4 w}{\partial y^4}\right)\left\{\frac{D_{11}A_{11}-B_{11}^2}{A_{11}}\right\}- \\ &N_{xx}^T\frac{\partial^2 w}{\partial x^2}-N_{yy}^T\frac{\partial^2 w}{\partial x^2}+\frac{\partial^2 w}{\partial x^2}\times \\ &\int_0^a\int_0^b\left(\begin{array}{l} A_{11}\frac{1}{2}\left(\frac{\partial w}{\partial x}\right)^2+A_{12}\frac{1}{2}\left(\frac{\partial w}{\partial y}\right)^2- \\ B_{11}\frac{\partial^2 w}{\partial x^2}-B_{12}\frac{\partial^2 w}{\partial y^2} \end{array}\right)\mathrm{d}x\,\mathrm{d}y \\ &+\frac{\partial^2 w}{\partial y^2}\int_0^a\int_0^b\left(\begin{array}{l} A_{12}\frac{1}{2}\left(\frac{\partial w}{\partial x}\right)^2+A_{22}\frac{1}{2}\left(\frac{\partial w}{\partial y}\right)^2- \\ B_{12}\frac{\partial^2 w}{\partial x^2}-B_{22}\frac{\partial^2 w}{\partial y^2} \end{array}\right)\mathrm{d}x\,\mathrm{d}y+ \\ &2\frac{\partial^2 w}{\partial x\,\partial y}\int_0^a\int_0^b\left(A_{66}\frac{\partial w}{\partial x}\frac{\partial w}{\partial y}-2B_{66}\frac{\partial^2 w}{\partial x\,\partial y}\right)\mathrm{d}x\,\mathrm{d}y+I_0\frac{\partial^2 w}{\partial t^2} \end{aligned} \tag{22}$$

$$+2q\left[\begin{array}{l}\dfrac{1}{M}\left(\dfrac{1}{U}\dfrac{\partial w}{\partial t}+\dfrac{\partial w}{\partial x}\cos\Lambda+\dfrac{\partial w}{\partial y}\sin\Lambda\right)+\\ \dfrac{\gamma+1}{4}\left(\dfrac{1}{U}\dfrac{\partial w}{\partial t}+\dfrac{\partial w}{\partial x}\cos\Lambda+\dfrac{\partial w}{\partial y}\sin\Lambda\right)^2+\\ \dfrac{\gamma+1}{12}M\left(\dfrac{1}{U}\dfrac{\partial w}{\partial t}+\dfrac{\partial w}{\partial x}\cos\Lambda+\dfrac{\partial w}{\partial y}\sin\Lambda\right)^3\end{array}\right]=0$$

For the sake of convenience, the following dimensionless parameters can be introduced as follows:

$$\begin{aligned}&W=\frac{w}{h},\quad \xi=\frac{x}{a},\quad \eta=\frac{y}{b},\quad \lambda=\frac{2q_\infty a^3}{\beta D_m},\quad \mu=\frac{\rho_\infty a}{\rho_m h},\\ &\tau=t\left(\frac{D_m}{\rho_m h a^4}\right)^{1/2},\quad R_x=\frac{N_{xx}^T a^2}{D_m},\quad R_x=\frac{N_{yy}^T b^2}{D_m}\end{aligned}\tag{23}$$

Subsequently, by substituting Eq. (33) into Eq. (32), the dimensionless form of the equation can be obtained as:

$$\begin{aligned}&\left(\frac{\partial^4 W}{\partial\xi^4}+2\left(\frac{a}{b}\right)^2\frac{\partial^4 W}{\partial\xi^2\partial\eta^2}+\left(\frac{a}{b}\right)^4\frac{\partial^4 W}{\partial\eta^4}\right)\left\{\frac{D_{eq}}{D_m}\right\}+\\ &\quad\frac{I_0}{\rho_m h}\frac{\partial^2 W}{\partial\tau^2}-R_x\frac{\partial^2 W}{\partial\xi^2}-R_y\left(\frac{a}{b}\right)^2\frac{\partial^2 W}{\partial\eta^2}-\\ &\quad R_x\frac{\partial^2 W}{\partial\xi^2}-R_y\left(\frac{a}{b}\right)^4\frac{\partial^2 W}{\partial\eta^2}+\\ &\frac{\partial^2 W}{\partial\xi^2}\int_0^1\int_0^1\left[\begin{array}{l}A_{11}\dfrac{abh^2}{2D_m}\left(\dfrac{\partial W}{\partial\xi}\right)^2+A_{12}\dfrac{a^3h^3}{2bD_m}\left(\dfrac{\partial W}{\partial\eta}\right)^2\\ -B_{11}\dfrac{abh}{D_m}\dfrac{\partial^2 W}{\partial\xi^2}-B_{12}\dfrac{a^3h^3}{bD_m}\dfrac{\partial^2 W}{\partial\eta^2}\end{array}\right]\mathrm{d}\xi\mathrm{d}\eta+\\ &\frac{\partial^2 w}{\partial\eta^2}\int_0^a\int_0^b\left[\begin{array}{l}A_{12}\dfrac{a^3h^3}{2bD_m}\left(\dfrac{\partial W}{\partial\xi}\right)^2+A_{22}\dfrac{abh^2}{2D_m}\left(\dfrac{\partial W}{\partial\eta}\right)^2\\ -B_{12}\dfrac{a^3h}{bD_m}\dfrac{\partial^2 W}{\partial\xi^2}-B_{22}\dfrac{abh}{D_m}\dfrac{\partial^2 W}{\partial\eta^2}\end{array}\right]\mathrm{d}\xi\mathrm{d}\eta+\\ &2\frac{\partial^2 W}{\partial\xi\partial\eta}\int_0^1\int_0^1\left[A_{66}\frac{a^3h^2}{bD_m}\frac{\partial W}{\partial\xi}\frac{\partial W}{\partial\eta}-2B_{66}\frac{a^3h}{bD_m}\frac{\partial^2 W}{\partial\xi\partial\eta}\right]\mathrm{d}\xi\mathrm{d}\eta+\\ &\frac{M\lambda h(\gamma+1)}{12a}\left(\frac{\partial W}{\partial\xi}\cos\Lambda+\left(\frac{\mu}{\lambda M}\right)^{1/2}\frac{\partial W}{\partial\tau}+\frac{\partial W}{\partial\eta}\sin\Lambda\right)^3+\\ &\frac{M\lambda h(\gamma+1)}{4a}\left(\frac{\partial W}{\partial\xi}\cos\Lambda+\left(\frac{\mu}{\lambda M}\right)^{1/2}\frac{\partial W}{\partial\tau}+\frac{\partial W}{\partial\eta}\sin\Lambda\right)^2+\\ &\lambda\left(\frac{\partial W}{\partial\xi}\cos\Lambda+\left(\frac{\mu}{\lambda M}\right)^{1/2}\frac{\partial W}{\partial\tau}+\frac{\partial W}{\partial\eta}\sin\Lambda\right)=0\end{aligned}\tag{24}$$

The boundary conditions considered here for the four edges are simply supported and are given by

$$\begin{aligned}&\frac{\partial^2 W}{\partial\xi^2}\Big|_{\xi=0,1}=0,\qquad W\Big|_{\xi=0,1}=0\\ &\frac{\partial^2 W}{\partial\eta^2}\Big|_{\eta=0,1}=0,\qquad W\Big|_{\eta=0,1}=0\end{aligned}\tag{25}$$

4- Solution Procedure

The Generalized Differential Quadrature Method (GDQM) provides accurate results with lower computational efforts compared to the analytical/semi-analytical methods. Therefore, in the present study, GDQM is applied to discretize the aeroelastic equation. The derivative of a function for spatial variables at a discrete point is approximated by a weighted linear sum of the function values at all discrete points in the solution domain [40]. The following relations are valid for the r-th derivative of a function $W(s)$, which is calculated as:

$$\frac{\partial^r W}{\partial s^r}\Big|_{s=s_i}=\sum_{j=1}^{N}A_{ij}^r W_J\tag{26}$$

where N is the number of grid points, $A_{ij}^{(r)s}$ represent the weighting coefficients of the summation, which can be obtained for the first-order derivatives as follows:

$$A_{ij}^{(1)}=\begin{cases}\dfrac{\bar{M}_x^{(1)}(x_i)}{(x-x_i)\bar{M}_x^{(1)}(x_k)}\\ \quad\text{for}\quad i\neq k\quad\text{and}\quad i,k=1,2,...N\\ -\sum\limits_{s=1,s\neq i}^{N}c_{is}^{(1)}\\ \quad\text{for}\quad i=k\quad\text{and}\quad i,k=1,2,...N\end{cases}\tag{27}$$

where the function $\bar{M}$ and the derivatives of it are given by:

$$\begin{aligned}&\bar{M}_x(x)=\prod_{s=1}^{N}(x-x_s),\\ &\bar{M}_x^{(1)}(x)=\prod_{s=1,s\neq j}^{N}(x-x_s)\end{aligned}\tag{28}$$

To obtain weighting coefficients of linear combinations of partial derivatives and integrals, the following relationships would be utilized [41].

$$\frac{\partial^{(r+s)}W}{\partial x^r\partial y^s}=\sum_{k=1}^{N}\sum_{l=1}^{M}A_{ik}^r A_{jl}^s W_{kl}\tag{29}$$

$$\int_0^a\int_0^b W(x,y)\mathrm{d}x\mathrm{d}y=\sum_{k=1}^{N}\sum_{l=1}^{M}A_{ik}^r c_k c_l W_{kl}\tag{30}$$

which c_l and c_k are calculated as:

$$c_k=H_{jk}^{I(x)}-H_{ik}^{I(x)}=\int_0^a r_k(x)\mathrm{d}x\tag{31}$$

$$c_l = H_{jl}^{I(y)} - H_{il}^{I(y)} = \int_0^b r_r(y)\mathrm{d}y \tag{32}$$

$$\begin{aligned} H^{I(x)} &= (A^{(1)x})^{-1}, \\ H^{I(y)} &= (A^{(1)y})^{-1} \end{aligned} \tag{33}$$

The coupled nonlinear Partial Differential Equations (PDE) are reduced into nonlinear Ordinary Differential Equations (ODE) by the DQM method.

$$\begin{aligned}
&\frac{I_0}{\rho_m h}\ddot{W} + \frac{D_{eq}}{D_m}\left(\begin{array}{l}\sum_{k1=1}^{N} Ax_{ik1}^{(4)} W_{k1j} + \\ 2\left(\frac{a}{b}\right)^2 \sum_{k1=1}^{N}\sum_{k2=1}^{M} Ay_{ik1}^{(2)} Ay_{jk2}^{(2)} W_{k1k2} + \\ \left(\frac{a}{b}\right)^4 \sum_{k2=1}^{M} Ay_{jk2}^{(4)} W_{ik2}\end{array}\right) + \\
&A_{11}\frac{abh^2}{2D_m}\sum_{k,l,m,n=1}^{N}\sum_{p=1}^{M} c_k c_p A_{kn}^{(1)x} A_{pm}^{(1)x} A_{il}^{(2)x} W_{kn} W_{pm} W_{lj} + \\
&A_{12}\frac{a^3h^2}{2bD_m}\sum_{k,l=1}^{N}\sum_{p,q,s=1}^{M} c_k c_p A_{kq}^{(1)y} A_{ps}^{(1)y} A_{il}^{(2)x} W_{kq} W_{ps} W_{lj} - \\
&B_{11}\frac{abh}{D_m}\sum_{k,l,n=1}^{N}\sum_{p=1}^{M} c_k c_p A_{kn}^{(2)x} A_{il}^{(2)x} W_{pn} W_{lj} - \\
&B_{12}\frac{a^3h}{bD_m}\sum_{k,l=1}^{N}\sum_{p,q=1}^{M} c_k c_p A_{pq}^{(2)y} A_{il}^{(2)x} W_{kq} W_{lj} + \\
&2A_{66}\frac{a^3h^2}{bD_m}\sum_{k,k1,n=1}^{N}\sum_{p,k2,q=1}^{M} c_k c_p A_{kn}^{(1)x} A_{pq}^{(1)y} A_{ik1}^{(1)x} A_{jk2}^{(1)y} W_{kn} W_{pq} W_{k1k2} - \\
&4B_{66}\frac{a^3h}{bD_m}\sum_{k,k1,n=1}^{N}\sum_{p,k2,q=1}^{M} c_k c_p A_{kn}^{(1)x} A_{pq}^{(1)y} A_{ik1}^{(1)x} A_{jk2}^{(1)y} W_{nq} W_{k1k2} + \\
&A_{12}\frac{a^3h^2}{2bD_m}\sum_{k=1}^{N}\sum_{p,q,t,s=1}^{M} c_k c_p A_{ks}^{(1)x} A_{pt}^{(1)x} A_{jq}^{(2)y} W_{ks} W_{pt} W_{iq} + \\
&A_{22}\frac{abh^2}{2D_m}\sum_{k,m,n=1}^{N}\sum_{p,q=1}^{M} c_k c_p A_{pm}^{(1)y} A_{kn}^{(1)y} A_{jq}^{(2)y} W_{pm} W_{kn} W_{iq} - \\
&B_{12}\frac{a^3h}{bD_m}\sum_{k=1}^{N}\sum_{p,q,t=1}^{M} c_k c_p A_{pt}^{(2)x} A_{jq}^{(2)y} W_{kt} W_{iq} - \\
&B_{22}\frac{abh}{D_m}\sum_{k,n=1}^{N}\sum_{p,q=1}^{M} c_k c_p A_{kn}^{(2)y} A_{jq}^{(2)y} W_{pn} W_{iq} - \\
&R_x\sum_{k1=1}^{N} A_{ik1}^{(2)x} W_{k1j} - R_y\left(\frac{a}{b}\right)^4\sum_{k2=1}^{M} A_{jk2}^{(2)y} W_{ik2} + \\
&\lambda\left(\sum_{k1=1}^{N} A_{ik}^{(1)x} W_{k1j} + \left(\frac{\mu}{\lambda M}\right)^{1/2}\dot{W}\right) + \\
&\lambda\left(M\frac{h}{a}\right)\frac{\gamma+1}{4}\left(\sum_{k1=1}^{N} A_{ik}^{(1)x} W_{k1j} + \left(\frac{\mu}{\lambda M}\right)^{1/2}\dot{W}\right)^2 + \\
&\lambda\left(M\frac{h}{a}\right)^2\frac{\gamma+1}{12}\left(\sum_{k1=1}^{N} A_{ik}^{(1)x} W_{k1j} + \left(\frac{\mu}{\lambda M}\right)^{1/2}\dot{W}\right)^3 = 0
\end{aligned} \tag{34}$$

for $i,k,l,m,n,k1 = 1,2,...,N$
and $j,p,q,s,t,k2 = 1,2,...,M$

By incorporating the boundary conditions into Eq. (34) and doing some manipulations, the final equation can be expressed as:

$$\begin{aligned}
&\frac{\ddot{W}\,I_0}{\rho_m h} + \frac{D_{eq}}{D_m}\left(\begin{array}{l}\sum_{k=3}^{N-2} d_1 W_{kj} + \left(\frac{a}{b}\right)^4\sum_{k=3}^{M-2} d_3 W_{ik} + \\ 2\left(\frac{a}{b}\right)^2\sum_{k1=3}^{N-2}\sum_{k2=3}^{M-2} d_2 W_{k1k2}\end{array}\right) + \\
&A_{11}\frac{abh^2}{2D_m}\sum_{k,l,m,n=3}^{N-2}\sum_{p=3}^{M-2} d_4 W_{kn} W_{pm} W_{lj} + \\
&A_{12}\frac{a^3h^2}{2bD_m}\sum_{k,l=3}^{N-2}\sum_{m,n,p=3}^{M-2} d_5 W_{kp} W_{mn} W_{lj} - \\
&B_{11}\frac{abh}{D_m}\sum_{k,l,n=3}^{N-2}\sum_{p=3}^{M-2} d_6 W_{pn} W_{lj} - \\
&B_{12}\frac{a^3h}{bD_m}\sum_{k,l=3}^{N-2}\sum_{p,q=3}^{M-2} d_7 W_{kq} W_{lj} + \\
&2A_{66}\frac{a^3h^2}{bD_m}\sum_{k,k1,n=3}^{N-2}\sum_{p,k2,q=3}^{M-2} d_8 W_{kn} W_{pq} W_{k1k2} - \\
&4B_{66}\frac{a^3h}{bD_m}\sum_{k,k1,n=3}^{N-2}\sum_{p,k2,q=3}^{M-2} d_9 W_{nq} W_{k1k2} + \\
&A_{12}\frac{a^3h^2}{2bD_m}\sum_{k=3}^{N-2}\sum_{p,q,t,s=3}^{M-2} d_{10} W_{ks} W_{pt} W_{iq} + \\
&A_{22}\frac{abh^2}{2D_m}\sum_{k,m,n=3}^{N-2}\sum_{p,q=3}^{M-2} d_{11} W_{pm} W_{kn} W_{iq} - \\
&B_{12}\frac{a^3h}{bD_m}\sum_{k=3}^{N-2}\sum_{p,q,t=3}^{M-2} d_{12} W_{kt} W_{iq} - \\
&B_{22}\frac{abh}{D_m}\sum_{k,n=3}^{N-2}\sum_{p,q=3}^{M-2} d_{13} W_{pn} W_{iq} - \\
&R_x\sum_{k=3}^{N-2} d_{14} W_{kj} - R_y\left(\frac{a}{b}\right)^4\sum_{k=3}^{M-2} d_{15} W_{ik} + \\
&\lambda\left(\sum_{k1=1}^{N} d_{16} W_{k1j} + \left(\frac{\mu}{\lambda M}\right)^{1/2}\dot{W}\right) + \\
&\lambda\left(M\frac{h}{a}\right)\frac{\gamma+1}{4}\left(\sum_{k1=1}^{N} d_{16} W_{k1j} + \left(\frac{\mu}{\lambda M}\right)^{1/2}\dot{W}\right)^2 + \\
&\lambda\left(M\frac{h}{a}\right)^2\frac{\gamma+1}{12}\left(\sum_{k1=1}^{N} C_{16} W_{k1j} + \left(\frac{\mu}{\lambda M}\right)^{1/2}\dot{W}\right)^3 = 0
\end{aligned} \tag{35}$$

The constant coefficients are defined in Appendix.

5- Numerical Results and Discussion

All the above-mentioned details on algorithms and formulations are adopted in a single code. All the calculation codes are compiled and implemented through MATLAB software. In what follows, convergence and accuracy of aeroelastic behaviors of FG plates are presented. The FGM

Table 1. Temperature dependent coefficients of Si3N3 (ceramic) and SUS304 (metal).

Material	Properties	P_0	P_{-1}	P_1	P_2	P_3
SUS304	E(Pa)	201.04E9	0	3.079E-4	-6.534E-7	0
	α(1/K)	1.23E-5	0	8.086E-4	0	0
Si_3N_3	E(Pa)	348.43E9	0	-3.07E-4	2.16E-7	-8.946E-11
	α(1/K)	5.8723E-6	0	9.095E-4	0	0

Table 2. Converge of critical dimensionless dynamic pressure

	λ_{cr}				
sampling points	n=0	n=0.5	n=1	n=5	n=*inf*
7×7	718.47	609.59	575.02	517.92	443.76
9×9	714.34	605.16	566.87	510.32	438.05
11×11	714.26	605.08	566.79	510.16	437.90
13×13	714.23	605.07	566.78	510.13	437.89
15×15	714.22	605.07	566.77	510.13	437.89

Table 3. Comparison of critical dimensionless dynamic pressure

	λ_{cr}				
Volume fraction	n=0	n=0.5	n=1	n=5	n=inf
Present	792.81	682.50	642.82	586.25	512.13
Sohn and Kim [8]	792.7	681.4	641.3	584.9	511.1

is made of Si_3N_3 and SUS304 with material properties given in Table 1.

In order to determine the minimum required number of sampling points, the convergence study is presented in Table 2. As seen from this table, convergence is achieved considering 11×11 sampling points in the computational domain. So at the rest of the manuscript and in all of the numerical results and evaluations, only 11×11 sampling points in the computational domain will be considered.

By using 11×11 sampling points in the computational domain, the governing aerothermoelastic equation was solved to evaluate the flutter instability [42]. It should be noted the sampling point distribution plays a key role in the nonlinear analysis [23]. The numerical simulations are obtained by fourth-order Runge–Kutta method and the nonlinear aeroelastic equations of the FG plate are analyzed to identify the Limit Cycle Oscillation (LCO) and complex chaotic behaviors of the system.

5- 1- Structural and aeroelastic model verification

The comparison study is accomplished between the obtained results of this research and the results reported by Sohn and Kim [8] which studied the dynamic stabilities of Functionally Graded (FG) panels that are subjected to combined thermal and aerodynamic loads. They used the Newton–Raphson method to obtain solutions of the nonlinear governing equations. The characteristics of the system are: a/b=1(aspect ratio), a/h=100 (length/ thickness ratio). Table 3 shows a good agreement for different values of volume fraction exponent in this comparison, which indicates that the proposed method and formula derivation are valid.

The second comparative study is devoted to the amplitudes of LCOs at $\zeta = 0.75$ and $\eta = 0.5$ in supersonic airflow for an FGM square plate. Figure. 2 shows good agreement between the results of the present work and Navazi and Haddadpour [21]. We can see that the present method has good accuracy and reliability to deal with the flutter behavior of the FGM plate.

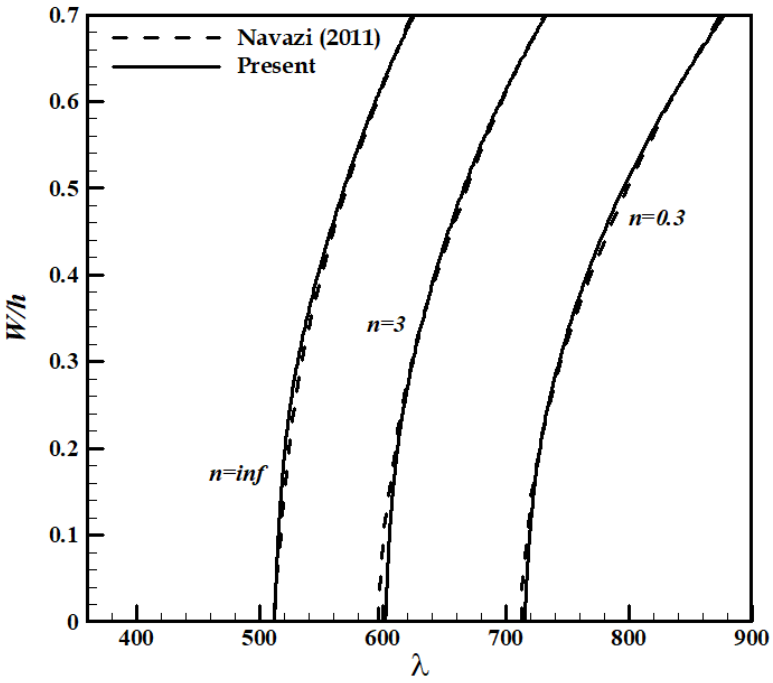

Fig. 2. LCO amplitudes of an FG plate in supersonic airflow.

Table 4. Critical dimensionless dynamic pressure for different porosity coefficients and porosity distributions

Volume fraction		λ_{cr}				
		n=0	n=0.5	n=1	n=5	n=inf
Perfect	α=0.0	792.81	682.50	642.82	586.25	512.13
Even	α=0.1	714.26	605.08	566.79	510.16	437.90
	α=0.2	641.21	532.81	498.24	438.87	368.55
Uneven	α=0.1	771.48	661.13	620.89	565.23	491.61
	α=0.2	752.34	642.19	603.71	546.68	473.63

5- 2- Aeroelastic stability analysis

Table 4 presents critical dimensionless dynamic pressure for different porosity coefficients and porosity distributions. For both distributions, it is found that the critical dimensionless dynamic pressure of porous plates decreases with increasing porosity coefficient (α). It is concluded from these tables that, even the porosity model has a greater effect on critical dimensionless dynamic pressure. Fig. 3 shows the dimensionless dynamic pressure with the flow yaw angle for different porosity coefficients and porosity distributions. It can be known from the figure that with the change of the flow yaw angle, the dimensionless dynamic pressure increases first and then decreases for the flow yaw angle of 0 and 90°.

In this examination, the amount of angle increase is equal to 3 degrees. From Fig. 3 it can be seen that the maximum difference of dimensionless dynamic pressure is obtained with the flow yaw angle equal to 45 degrees. Besides, uneven porosity distribution leads to more stabilized configurations compared with the even porous model.

This is since the porosities in the even model are regularly distributed through the thickness of the plate, whereas in the uneven model, porosities are particularly distributed close to the middle surface of the plate. A final remark is that the dimensionless dynamic pressure increases with decreasing of the top surface temperature of the plate (T_c) for the same volume fractions.

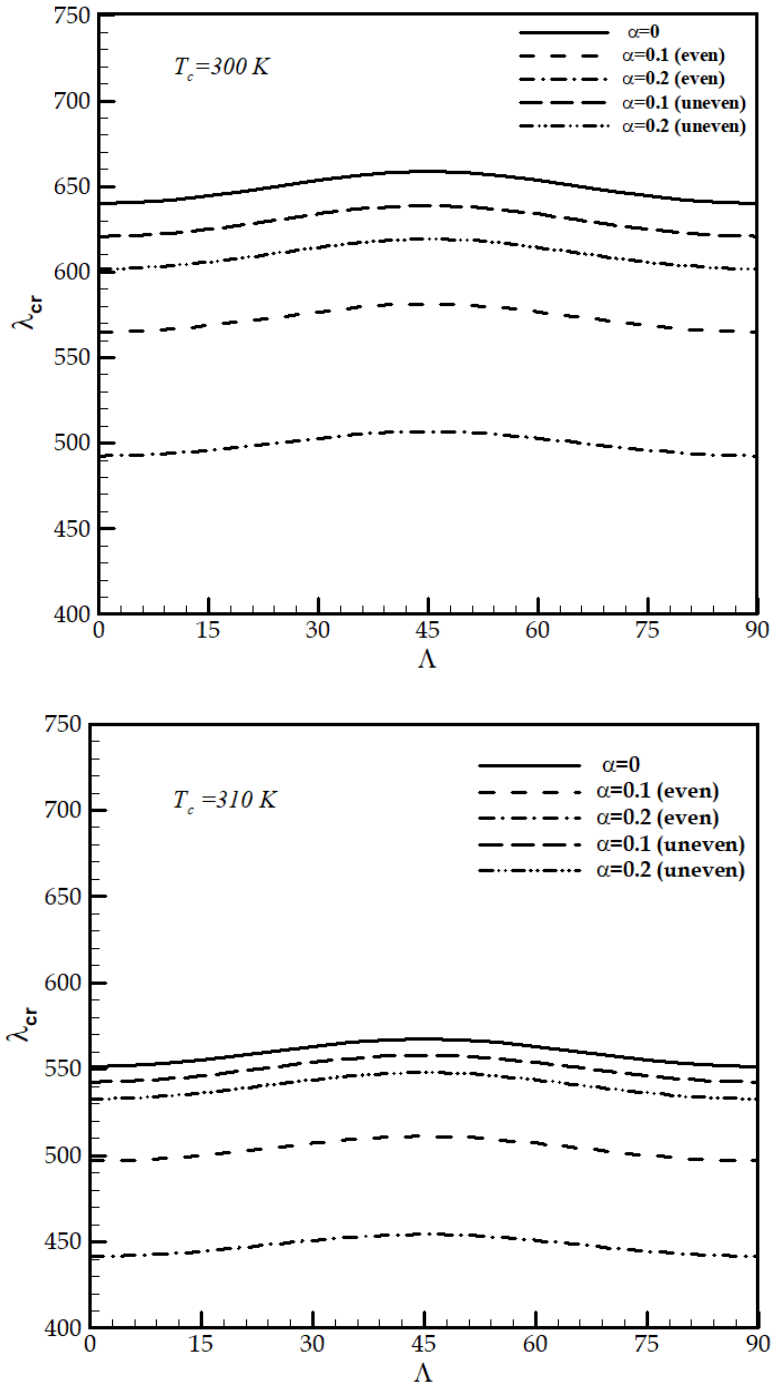

Fig. 3. LCO Dimensionless critical flutter pressure with change in flow yaw angle for n =1.

5- 3- Nonlinear flutter analysis

To observe the effects of upper surface temperature (ceramic) and porosity simultaneously on the aerothermoelastic behavior of FG plate, the bifurcation diagrams plotting the maximum deflection amplitude at the gauge point versus the upper surface temperature for perfect (α=0), even porous (α=0.1) and uneven (α =0.1) with two value in yaw angle (Λ=0, 30^0) are plotted in Fig. 4. To this end, for each case the variation of the critical free-stream pressure is obtained by increasing the outer surface temperature, T_c, while the bottom surface temperature, T_m is defined as the reference temperature and equal to 300 K. Accordingly, it is expected that the temperature-dependent material variation decreases the critical flutter dynamic pressure. At low temperatures, the plate is aeroelastic stable. The plate can oscillate for some time when disturbed, but the damping will finally dissipate the motion. The temperature rise will cause a decrease in the structural rigidity of the FG plate. As shown in Fig. 4, the temperature-dependent material variation increases flutter instability and asymmetric limit cycle oscillation occurs and the amplitudes will continue to rise with the increase in the change rates of the material mechanical properties.

It is obvious that as the temperature increases, simple LCO with the harmonic motion becomes an asymmetric limit cycle oscillation, and with more increases to come narrow-band chaotic motion and wide-band chaotic motion. At first sight, one may observe that porosity coefficients have a major influence on the stability margins and chaotic motions. It can be seen that for both porosity distributions, the chaotic behavior appears in higher temperatures but even porosity distribution may lead to more reduction in the start of chaotic motion. It should be stated that the effective stiffness to effective mass ratio is the highest at uneven models. Based on the reported results, as the flow yaw angle increases, the wide-band chaotic motion happens at the higher value of upper surface temperature.

The phase plots corresponding to different upper surface temperature (Δ_c) with even porosity α=0.1, Λ=30, λ=400, M=5, and n =1 in gauge point are shown in Fig. 5. Firstly, the plate undergoes simple LCO and after that, with further Δc multiple periodic motions occur.

Considering a slight change in Δc structural nonlinearity remarkably enhances with the rise of temperature and the amplitude of simple LCO increase Bifurcation diagram of FG plate with even porosity under increasing dimensionless dynamic pressure (λ) for various yaw angles (Λ), with M=6, T_c=T_m=300, and n =10 are calculated and shown in Fig. 6. It is found that by increasing porosity coefficient (α) the bifurcation point shifts to the left side of the bifurcation diagram and flutter occurs at the lower value of dimensionless dynamic pressure. According to the illustrated plot in Fig. 6, increasing porosity coefficient lead to an increase of the harmonic oscillation amplitude, and also this phenomenon shifts to the left side of this diagram. The last finding is that by increasing dimensionless dynamic pressure, the harmonic oscillation amplitude decreases. To deeper understanding, Fig. 7 illustrates nonlinear flutter response and phase diagram for different values of dimensionless pressure with Λ=0, α=0.2, M=6, and n =10. It is observed from Fig. 7 that at λ = 700, the oscillation of the plate is an LCO whose dimensionless amplitude is 1.3. By increasing the dimensionless pressure the motion of the plate is still an LCO, but the amplitude increases to 1.5. Gradually increasing the dimensionless pressure to λ = 1000, the chaotic motion of the plate occurs. It is interesting that at λ= 1100, wide-band chaotic motion changes to narrowband chaotic motion.

6- Conclusion

In this study, the nonlinear flutter characteristics of the porous FGM, under simultaneous actions of the thermal Loads and yawed hypersonic airflow are investigated. The governing equations are obtained using Von Karman's large deflection and third-order piston theory. The material properties of the plate are assumed to vary across the thickness direction according to a simple power-law distribution. Two types of FG porous distributions, namely even porosity and uneven porosity distribution were considered in this paper. The nonlinear geometric partial differential equations due to the stretching effect have been expressed by assumptions with Von Karman's strain-displacement relation to obtain unsteady aerodynamic pressure in the hypersonic regime. Hamilton's principle is employed method, the non-linear aerothermoelastic equation is transferred to ordinary differential equations. Based on the generalized differential quadrature method, the nonlinear aerothermoelastic equation is transferred to ordinary differential equations. Moreover, the assumed mode method along with the Runge-Kutta integration algorithm is used as a solution method. Then, the influence of porosity distribution, porosity coefficient, and yawed flow angle were discussed in detail and the following conclusions can be made:

It is observed that the critical dimensionless dynamic pressure decreases with increasing both the volume fraction exponent and porosity coefficient.

Even porosity distribution would have a more destabilizing effect compared with the uneven porous model.

The maximum dimensionless dynamic pressure in even and uneven porosity models is obtained with the flow yaw angle equal to 45^o.

The dimensionless dynamic pressure increases with decreasing of the top surface temperature of the plate.

For both porosity distributions, the chaotic behavior appears in higher top surface temperature but even porosity distribution has a profound effect on chaotic motion.

As the flow yaw angle increases, the wide-band chaotic motion takes place at the higher value of the upper surface temperature of the plate.

The bifurcation diagram of the FG plate with even porosity under increasing λ shows, increasing porosity coefficient leads to an increase of the harmonic oscillation amplitude, and also this phenomena shifts to the left side of this diagram.

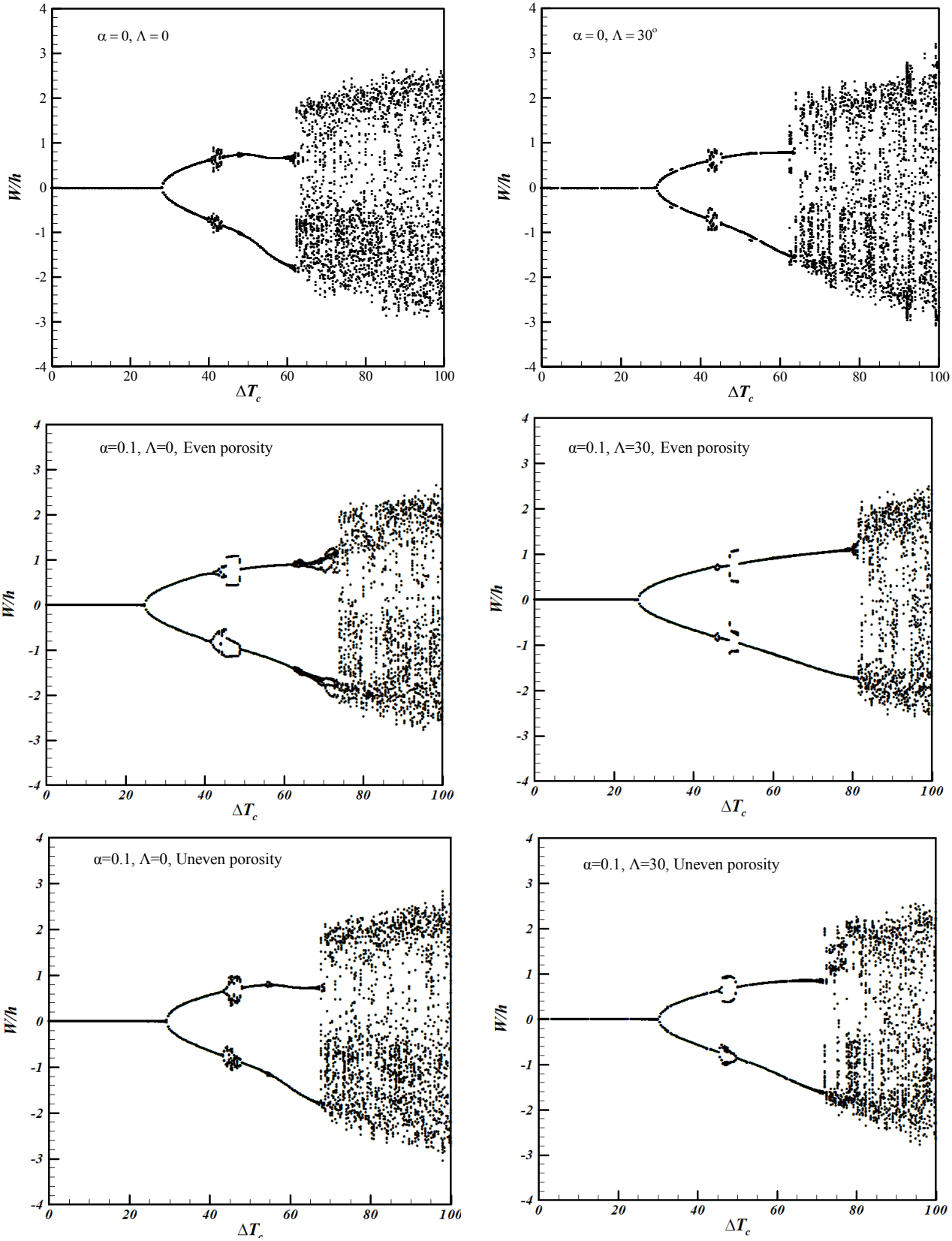

Fig. 4. Bifurcation diagram under increasing Tc for various yaw angles (Λ), with λ=400, M=5, and n =1.

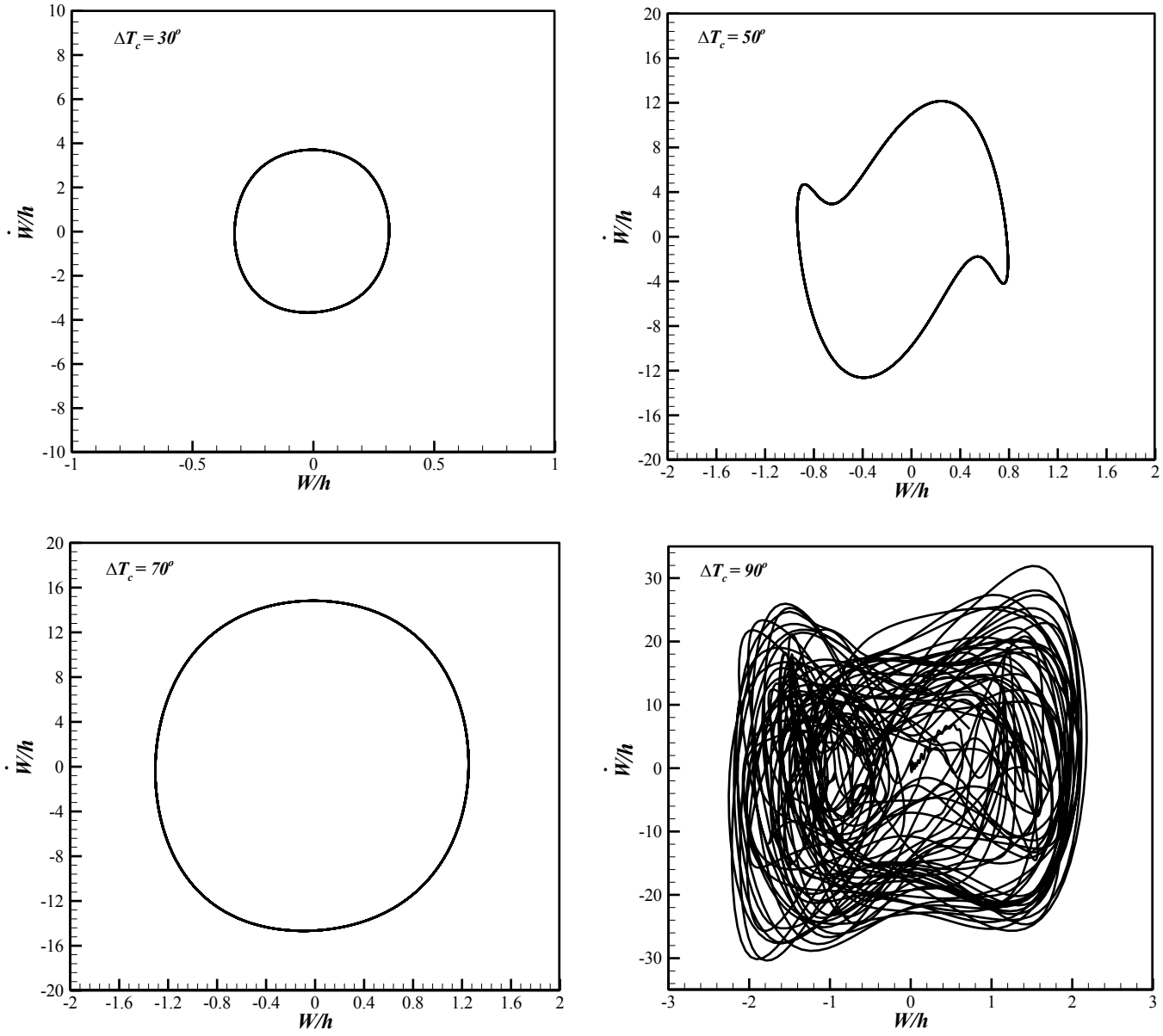

Fig. 5. Phase diagram of square FG plate with even porosity (α=0.1) in gauge point under varying upper surface temperature (Λ =30o, λ =400, M=5 and n =1)

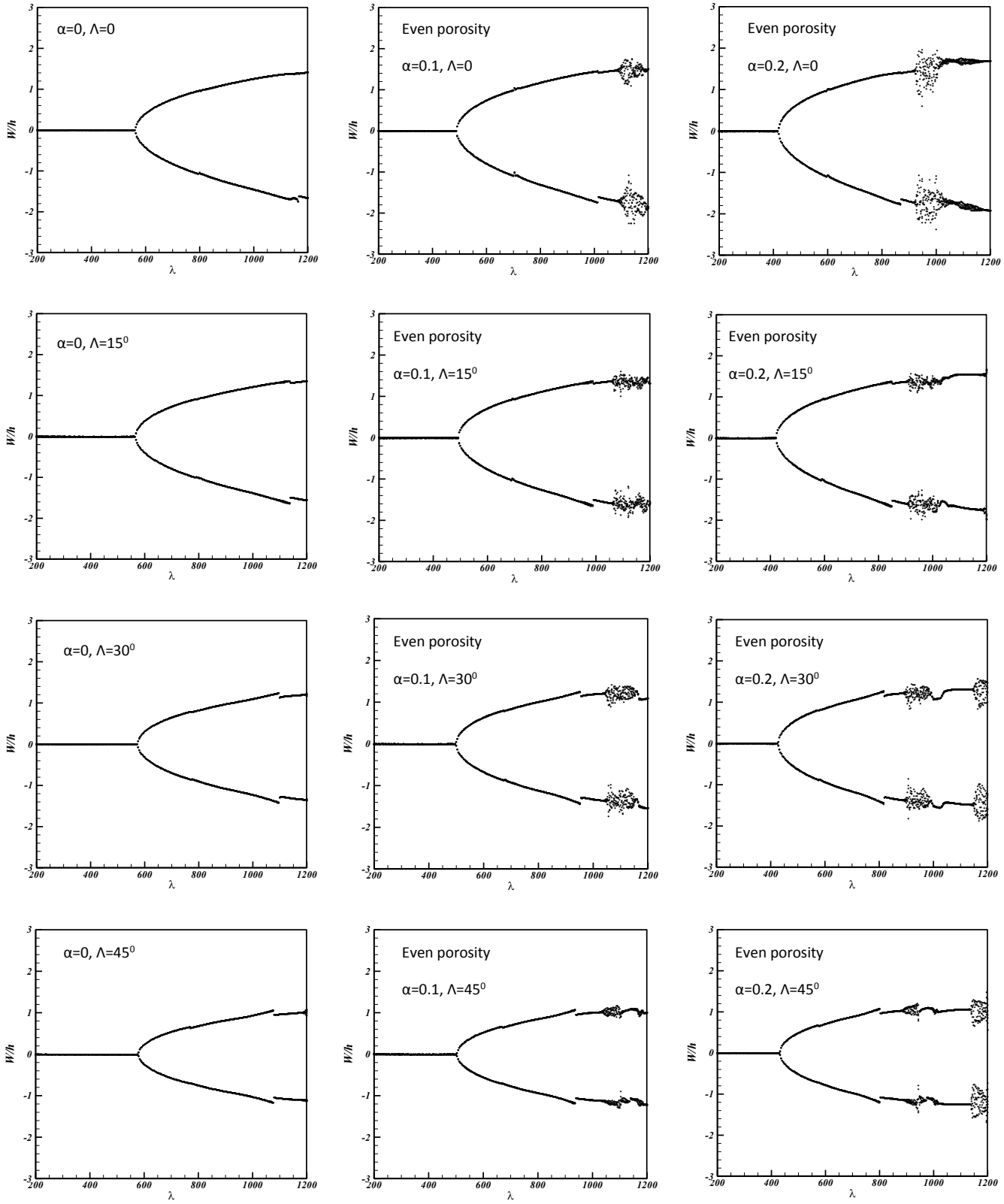

Fig. 6. Bifurcation diagram of FG plate with even porosity under increasing λ for various yaw angles (Λ) with M=6 and n =10.

Appendix

$$d_1 = A_{ik}^{(4)x} - \frac{A_{i,2}^{(4)x}.AXK1 + A_{i.N-1}^{(4)x}AXKN}{AXN}$$

$$d_2 = (A_{ik1}^{(2)x} - \frac{A_{i,2}^{(2)x}.AXK1 + A_{i.N-1}^{(2)x}AXKN}{AXN}) \times (A_{jk2}^{(2)y} - \frac{A_{j,2}^{(2)y}.AYK1 + A_{j.M-1}^{(2)y}AYKM}{AYM})$$

$$d_3 = (A_{jk}^{(4)y} - \frac{A_{j,2}^{(4)y}.AYK1 + A_{j.M-1}^{(4)y}AYKM}{AYM})$$

$$d_4 = c_k c_p (A_{kn}^{(1)x} - \frac{A_{k,2}^{(1)x}.AXK1 + A_{k.N-1}^{(1)x}AXKN}{AXN}) \times (A_{pm}^{(1)x} - \frac{A_{p,2}^{(1)x}.AXK1 + A_{p.N-1}^{(1)x}AXKN}{AXN}) \times (A_{il}^{(2)x} - \frac{A_{i,2}^{(2)x}.AXK1 + A_{i.N-1}^{(2)x}AXKN}{AXN})$$

$$d_5 = c_k c_p (A_{kq}^{(1)y} - \frac{A_{k,2}^{(1)y}.AYK1 + A_{k.M-1}^{(1)y}AYKM}{AYM}) \times (A_{ps}^{(1)y} - \frac{A_{p,2}^{(1)y}.AYK1 + A_{p,M-1}^{(1)y}AYKM}{AYM}) \times (A_{il}^{(2)x} - \frac{A_{i,2}^{(2)x}.AXK1 + A_{i.N-1}^{(2)x}AXKN}{AXN})$$

$$d_6 = c_k c_p (A_{kn}^{(2)x} - \frac{A_{k,2}^{(2)x}.AXK1 + A_{k.N-1}^{(2)x}AXKN}{AXN}) \times (A_{il}^{(2)x} - \frac{A_{i,2}^{(2)x}.AXK1 + A_{i.N-1}^{(2)x}AXKN}{AXN})$$

$$d_7 = c_k c_p (A_{pq}^{(2)y} - \frac{A_{p,2}^{(2)y}.AYK1 + A_{p,M-1}^{(2)y}AYKM}{AYM}) \times (A_{il}^{(2)x} - \frac{A_{i,2}^{(2)x}.AXK1 + A_{i.N-1}^{(2)x}AXKN}{AXN})$$

$$d_8 = c_k c_p (A_{kn}^{(1)x} - \frac{A_{k,2}^{(1)x}.AXK1 + A_{k.N-1}^{(1)x}AXKN}{AXN}) \times (A_{pq}^{(1)y} - \frac{A_{p,2}^{(1)y}.AYK1 + A_{p.M-1}^{(1)y}AYKM}{AYM}) \times (A_{ik1}^{(1)x} - \frac{A_{i,2}^{(1)x}.AXK1 + A_{i.N-1}^{(1)x}AXKN}{AXN}) \times (A_{jk2}^{(1)y} - \frac{A_{j,2}^{(1)y}.AYK1 + A_{j.M-1}^{(1)y}AYKM}{AYM})$$

$$d_9 = c_k c_p (A_{ks}^{(1)x} - \frac{A_{k,2}^{(1)x}.AXK1 + A_{k.N-1}^{(1)x}AXKN}{AXN}) \times (A_{pt}^{(1)y} - \frac{A_{p,2}^{(1)y}.AYK1 + A_{p.M-1}^{(1)y}AYKM}{AYM}) \times (A_{ik1}^{(1)x} - \frac{A_{i,2}^{(1)x}.AXK1 + A_{i.N-1}^{(1)x}AXKN}{AXN}) \times (A_{jk2}^{(1)y} - \frac{A_{j,2}^{(1)y}.AYK1 + A_{j.M-1}^{(1)y}AYKM}{AYM})$$

$$d_{10} = c_k c_p (A_{ks}^{(1)x} - \frac{A_{k,2}^{(1)x}.AXK1 + A_{k.N-1}^{(1)x}AXKN}{AXN}) \times (A_{pt}^{(1)x} - \frac{A_{p,2}^{(1)x}.AXK1 + A_{p.N-1}^{(1)x}AXKN}{AXN}) \times (A_{jq}^{(1)y} - \frac{A_{j,2}^{(1)y}.AYK1 + A_{j,M-1}^{(1)y}AYKM}{AYM})$$

$$d_{11} = c_k c_p (A_{pm}^{(1)y} - \frac{A_{p,2}^{(1)y}.AYK1 + A_{p,M-1}^{(1)y}AYKM}{AYM}) \times (A_{kn}^{(1)y} - \frac{A_{k,2}^{(1)y}.AYK1 + A_{k,M-1}^{(1)y}AYKM}{AYM}) \times (A_{jq}^{(2)y} - \frac{A_{j,2}^{(2)y}.AYK1 + A_{j,M-1}^{(2)y}AYKM}{AYM})$$

$$d_{12} = c_k c_p (A_{pt}^{(2)x} - \frac{A_{p,2}^{(2)x}.AXK1 + A_{p,N-1}^{(2)x}AXKN}{AXN}) \times (A_{jq}^{(2)y} - \frac{A_{j,2}^{(2)y}.AYK1 + A_{j,M-1}^{(2)y}AYKM}{AYM})$$

$$d_{13} = c_k c_p (A_{kn}^{(2)y} - \frac{A_{k,2}^{(2)y}.AYK1 + A_{k,M-1}^{(2)y}AYKM}{AYM}) \times (A_{jq}^{(2)y} - \frac{A_{j,2}^{(2)y}.AYK1 + A_{j,M-1}^{(2)y}AYKM}{AYM})$$

$$d_{14} = (A_{ik}^{(2)x} - \frac{A_{i,2}^{(2)x}.AXK1 + A_{i,N-1}^{(2)x}AXKN}{AXN})$$

$$d_{15} = (A_{jk}^{(2)y} - \frac{A_{j,2}^{(2)y}.AYK1 + A_{j,M-1}^{(2)y}AYKM}{AYM})$$

$$d_{16} = (A_{ik}^{(1)x} - \frac{A_{i,2}^{(1)x}.AXK1 + A_{i,N-1}^{(1)x}AXKN}{AXN})$$

Where

$$AXN = A^{(2)x}_{N,2}.A^{(2)x}_{1,N-1} - A^{(2)x}_{1,2}.A^{(2)x}_{N,N-1}$$

$$AXK1 = A^{(2)x}_{1,k}.A^{(2)x}_{N,N-1} - A^{(2)x}_{1,N-1}.A^{(2)x}_{N,k}$$

$$AXKN = A^{(2)x}_{1,2}.A^{(2)x}_{N,k} - A^{(2)x}_{1,k}.A^{(2)x}_{N,2}$$

$$AYN = A^{(2)y}_{M,2}.A^{(2)y}_{1,M-1} - A^{(2)y}_{1,2}.A^{(2)y}_{M,M-1}$$

$$AYK1 = A^{(2)y}_{1,k}.A^{(2)y}_{M,M-1} - A^{(2)y}_{1,M-1}.A^{(2)y}_{M,k}$$

$$AYKN = A^{(2)y}_{1,2}.A^{(2)y}_{M,k} - A^{(2)y}_{1,k}.A^{(2)y}_{M,2}$$

Author Contributions

M. Javadi: Conceptualization, Methodology, Writing-original draft, Writing-review & editing, Supervision. V. Khalafi: Methodology, Software, Validation.

Conflict of Interest

The author(s) declared no potential conflicts of interest with respect to the research, authorship, and publication of this article.

Funding

The author(s) received no financial support for the research, authorship, and publication of this article.

References

[1] H.-T. Thai, S.-E. Kim, A review of theories for the modeling and analysis of functionally graded plates and shells, Composite Structures, 128 (2015) 70-86.

[2] Z. Su, L. Wang, K. Sun, D. Wang, Vibration characteristic and flutter analysis of elastically restrained stiffened functionally graded plates in thermal environment, International Journal of Mechanical Sciences, 157 (2019) 872-884.

[3] M. Rahmanian, M. Javadi, A unified algorithm for fully-coupled aeroelastic stability analysis of conical shells in yawed supersonic flow to identify the effect of boundary conditions, Thin-Walled Structures, 155 (2020) 106910.

[4] W. Hayes, Hypersonic flow theory, Elsevier, 2012.

[5] E.H. Dowell, Aeroelasticity of plates and shells, Springer Science & Business Media, 1974.

[6] L.K. Abbas, C. Qian, P. Marzocca, G. Zafer, A. Mostafa, Active aerothermoelastic control of hypersonic double-wedge lifting surface, Chinese Journal of Aeronautics, 21(1) (2008) 8-18.

[7] T. Prakash, M. Ganapathi, Supersonic flutter characteristics of functionally graded flat panels including thermal effects, Composite structures, 72(1) (2006) 10-18.

[8] K.-J. Sohn, J.-H. Kim, Structural stability of functionally graded panels subjected to aero-thermal loads, Composite Structures, 82(3) (2008) 317-325.

[9] K.-J. Sohn, J.-H. Kim, Nonlinear thermal flutter of functionally graded panels under a supersonic flow, Composite Structures, 88(3) (2009) 380-387.

[10] G. Jiang, F. Li, Aerothermoelastic analysis of composite laminated trapezoidal panels in supersonic airflow, Composite Structures, 200 (2018) 313-327.

[11] V. Khalafi, J. Fazilati, Supersonic panel flutter of variable stiffness composite laminated skew panels subjected to yawed flow by using NURBS-based isogeometric approach, Journal of Fluids and Structures, 82 (2018) 198-214.

[12] Y. Chai, F. Li, Z. Song, C. Zhang, Influence of the boundary relaxation on the flutter and thermal buckling of composite laminated panels, Aerospace Science and Technology, 104 (2020) 106000.

[13] M. Rasool, M.K. Singha, Aeroelastic analysis of pre-stressed variable stiffness composite panels, Journal of Vibration and Control, 26(9-10) (2020) 724-734.

[14] P.K. Swain, N. Sharma, D.K. Maiti, B.N. Singh, Aeroelastic analysis of laminated composite plate with material uncertainty, Journal of Aerospace Engineering, 33(1) (2020) 04019111.

[15] X. Wang, Z. Yang, J. Zhou, W. Hu, Aeroelastic effect on aerothermoacoustic response of metallic panels in supersonic flow, Chinese Journal of Aeronautics, 29(6) (2016) 1635-1648.

[16] V.R. Kar, S.K. Panda, Nonlinear thermomechanical deformation behaviour of P-FGM shallow spherical shell panel, Chinese Journal of Aeronautics, 29(1) (2016) 173-183.

[17] P. Perlikowski, J. Warminski, S. Lenci, Recent advances in nonlinear dynamics and vibrations: special issue of meccanica, Meccanica, (2020) 1-5.

[18] L.-C. Shiau, L.-T. Lu, Nonlinear flutter of two-dimensional simply supported symmetric composite laminated plates, Journal of aircraft, 29(1) (1992) 140-145.

[19] H.H. Ibrahim, M. Tawfik, M. Al-Ajmi, Non-linear panel flutter for temperature-dependent functionally graded material panels, computational mechanics, 41(2) (2008) 325-334.

[20] M. Kouchakzadeh, M. Rasekh, H. Haddadpour, Panel flutter analysis of general laminated composite plates, Composite Structures, 92(12) (2010) 2906-2915.

[21] H. Navazi, H. Haddadpour, Nonlinear aero-thermoelastic analysis of homogeneous and functionally graded plates in supersonic airflow using coupled models, Composite Structures, 93(10) (2011) 2554-2565.

[22] Z.-G. Song, F.-M. Li, Aerothermoelastic analysis of nonlinear composite laminated panel with aerodynamic heating in hypersonic flow, Composites Part B: Engineering, 56 (2014) 830-839.

[23] H. Shahverdi, V. Khalafi, Bifurcation analysis of FG curved panels under simultaneous aerodynamic and thermal loads in hypersonic flow, Composite Structures, 146 (2016) 84-94.

[24] Y. Chai, F. Li, Z. Song, Nonlinear vibrations, bifurcations and chaos of lattice sandwich composite panels on Winkler–Pasternak elastic foundations with thermal effects in supersonic airflow, Meccanica, 54(7) (2019) 919-944.

[25] W. Xia, X. Zhao, D. Li, S. Shen, Nonlinear flutter response of pre-heated functionally graded panels, International Journal of Computational Materials Science and Engineering, 7(01n02) (2018) 1850012.

[26] L. Ye, Z. Ye, Aeroelastic Stability and Nonlinear Flutter Analysis of Heated Panel with Temperature-Dependent Material Properties, Journal of Aerospace Engineering, 33(6) (2020) 04020068.

[27] M. Rahmanian, M. Javadi, Supersonic Aeroelasticity and Dynamic Instability of Functionally Graded Porous Cylindrical Shells Using a Unified Solution Formulation, International Journal of Structural Stability and Dynamics, (2020) 2050132.

[28] M.-C. Trinh, D.-D. Nguyen, S.-E. Kim, Effects of porosity and thermomechanical loading on free vibration and nonlinear dynamic response of functionally graded sandwich shells with double curvature, Aerospace Science and Technology, 87 (2019) 119-132.

[29] M.R. Barati, H. Shahverdi, Aero-hygro-thermal stability analysis of higher-order refined supersonic FGM panels with even and uneven porosity distributions, Journal of Fluids and Structures, 73 (2017) 125-136.

[30] L. Hadji, M. Avcar, Free Vibration Analysis of FG Porous Sandwich Plates under Various Boundary Conditions, Journal of Applied and Computational Mechanics, (2020).

[31] N. Dinh Duc, V.D. Quang, P.D. Nguyen, T.M. Chien, Nonlinear dynamic response of functionally graded porous plates on elastic foundation subjected to thermal and mechanical loads, Journal of Applied and Computational Mechanics, 4(4) (2018) 245-259.

[32] K. Zhou, X. Huang, J. Tian, H. Hua, Vibration and flutter analysis of supersonic porous functionally graded material plates with temperature gradient and resting on elastic foundation, Composite Structures, 204 (2018) 63-79.

[33] R. Bahaadini, A.R. Saidi, K. Majidi-Mozafari, Aeroelastic flutter analysis of thick porous plates in supersonic flow, International Journal of Applied Mechanics, 11(10) (2019) 1950096.

[34] M. Rahmanian, T. Farsadi, H. Kurtaran, Nonlinear flutter of tapered and skewed cantilevered plates with curvilinear fiber paths, Journal of Sound and Vibration, 500 (2021) 116021.

[35] Y. Wang, C. Ye, J. Zu, Identifying the temperature effect on the vibrations of functionally graded cylindrical shells with porosities, Applied Mathematics and Mechanics, 39(11) (2018) 1587-1604.

[36] S.S. Rao, Vibration of continuous systems, Wiley Online Library, 2007.

[37] M. Amabili, Nonlinear vibrations and stability of shells and plates, Cambridge University Press, 2008.

[38] S.C. Dixon, M.L. Hudson, Flutter, vibration, and buckling of truncated orthotropic conical shells with generalized elastic edge restraint, National Aeronautics and Space Administration, 1970.

[39] M. Permoon, H. Haddadpour, M. Javadi, Nonlinear vibration of fractional viscoelastic plate: Primary, subharmonic, and superharmonic response, International Journal of Non-Linear Mechanics, 99 (2018) 154-164.

[40] M. Taskin, A. Arikoglu, O. Demir, Vibration and Damping Analysis of Sandwich Cylindrical Shells by the GDQM, AIAA Journal, (2019) 3040-3051.

[41] F. Tornabene, N. Fantuzzi, F. Ubertini, E. Viola, Strong formulation finite element method based on differential quadrature: a survey, Applied Mechanics Reviews, 67(2) (2015).

[42] H. Shahverdi, V. Khalafi, S. Noori, Aerothermoelastic analysis of functionally graded plates using generalized differential quadrature method, Latin American Journal of Solids and Structures, 13(4) (2016) 796-818.

HOW TO CITE THIS ARTICLE

M. Javadi, V. Khalafi, Nonlinear Flutter Analysis of Porous Functionally Graded Plate in Yawed Hypersonic Flow, AUT J. Mech Eng., 6(1) (2022) 59-76.

DOI: 10.22060/ajme.2021.19915.5972